Interference in strong-field ionization of a two-centre atomic system

To cite this article: Z Ansari *et al* 2008 *New J. Phys.* **10** 093027

View the article online for updates and enhancements.

Interference in strong-field ionization of a two-centre atomic system

Z Ansari[1], **M Böttcher**[1], **B Manschwetus**[1], **H Rottke**[1,6],
W Sandner[1], **A Verhoef**[2], **M Lezius**[2], **G G Paulus**[3],
A Saenz[4] **and D B Milošević**[5]

[1] Max-Born-Institut, Max-Born-Strasse 2A, D-12489 Berlin, Germany
[2] Max-Planck-Institut für Quantenoptik, Hans-Kopfermann-Strasse 1,
D-85748 Garching, Germany
[3] Institut für Optik und Quantenelektronik, Friedrich-Schiller-Universität Jena,
Max-Wien-Platz 1, D-07743 Jena, Germany
[4] Institut für Physik, Humboldt-Universität zu Berlin, Hausvogteiplatz 5-7,
D-10117 Berlin, Germany
[5] Faculty of Science, University of Sarajevo, Zmaja od Bosne 35,
71000 Sarajevo, Bosnia and Herzegovina
E-mail: rottke@mbi-berlin.de

Abstract. Strong-field photoionization of argon dimers by a few-cycle laser pulse is investigated using electron–ion coincidence momentum spectroscopy. The momentum distribution of the photoelectrons exhibits interference due to the emission from the two atomic argon centres, in analogy with a Young's double-slit experiment. However, a simulation of the dimer photoelectron momentum spectrum based on the atomic spectrum supplemented with a theoretically derived interference term leads to distinct deviations from the experimental result. The deviations may have their origin in a complex electron dynamics during strong-field ionization of the Ar_2 dimer.

[6] Author to whom any correspondence should be addressed.

IOP Institute of Physics Φ DEUTSCHE PHYSIKALISCHE GESELLSCHAFT

Contents

1. Introduction

The interference of particle waves separates the quantum world from everyday experience. The probability of finding a particle in space–time is determined by the coherent sum over all possible particle pathways from the source to that point. For two possible paths, interference is akin to that of light waves passing through a double slit, first described by Young [1]. Experiments with electrons [2], neutrons [3] and clusters [4] demonstrate that it is general to the quantum world, and that it can only be understood by the quantum nature of matter–wave duality, without reference to the macroscopic world. Similar to interference in optics, molecular electron emitters have been studied using electron [5] and ion impact ionization [6]–[9] or photoionization with a single high-energy photon [10]–[13]. Here, interference is of interest not only from a fundamental point-of-view, but also because photoelectron spectra and angular distributions are governed and modified by the emitter geometry [10]–[13].

Recently, quantum interference has gained considerable interest in strong-field photoionization using ultra-short high-intensity lasers. Double slits in time have been realized through electric-field ionization within sub-fs time windows in subsequent optical cycles [14]. Interference has been suggested to influence molecular [15, 16] and cluster [17] strong-field ionization. In its course it affects high-order harmonic generation [18, 19] and tomographic imaging of molecules [20]. To date, coherence in strong-field photoionization in the adiabatic limit has been studied for strongly bound molecules, where an electron is removed from a delocalized valence orbital. To isolate Young-type interference, on the other hand, it appears advantageous to start from a system consisting of two identical electron emitters placed at a fixed separation with minimized mutual interaction. In principle, inner-shell electrons of a molecule approach this situation [11]–[13], but they are not accessible to strong-field ionization at long wavelengths.

In order to investigate the effect of interference in strong-field ionization we therefore resort here to the loosely bound Ar_2 dimer. Noble gas dimers in general can be expected to behave virtually like two individual, nearly unperturbed coherent atomic emitters. A weak van der Waals potential bonds the two Ar atoms at an equilibrium internuclear separation $R \approx R_0 = 3.77\,\text{Å}$ in a $^1\Sigma_g^+$ electronic ground state with defined symmetry (figure 1) [21]. Ar_2 in particular can thus be expected to emit photoelectrons coherently from two nearly perfect unperturbed atomic centres.
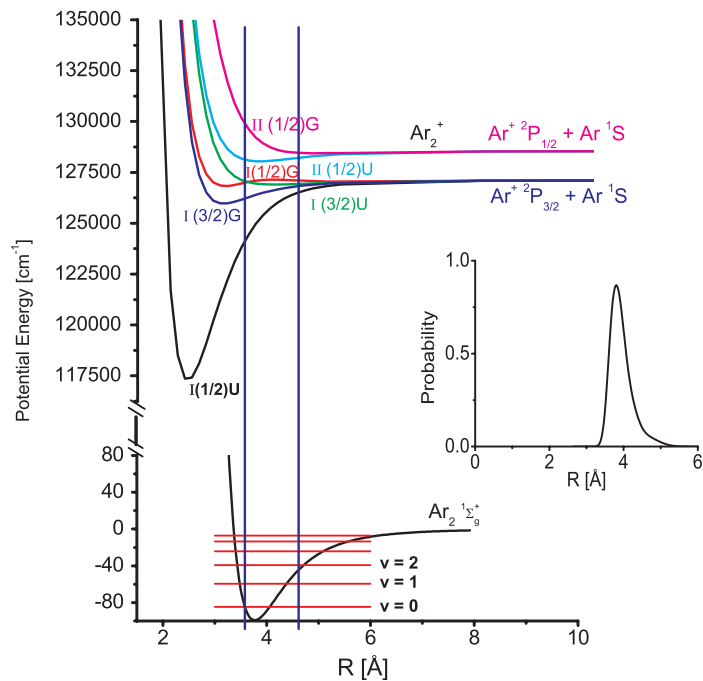
Figure 1. Potential energy curves for the ground state of Ar_2 and the low-lying electronic states of Ar_2^+ [21, 22]. The inset shows the initial distribution of Ar_2 internuclear separations of our dimer sample (temperature: $\approx 30\,K$). The two vertical lines limit the corresponding Franck–Condon regime for photoionization.

2. Experimental setup

A reaction microscope was used to investigate strong-field photoionization of the Ar_2 dimer (see figure 2). A detailed description of its principle of operation can be found in [23]. Ar_2 dimers were formed in a supersonic expansion of argon at a stagnation pressure of 3 bar and a gas temperature of $\approx 300\,K$ through a nozzle with a diameter of $20\,\mu m$. The supersonic beam consisted of a mixture of mainly Ar atoms and a small fraction of Ar_2 dimers (less than 2%). This dimer fraction which is estimated from our ion time-of-flight spectra is in good agreement with what one expects according to [24]. Under our expansion conditions the fraction of Ar_n clusters with $n > 2$ is estimated to be still negligible [24]. Based on the translational beam temperature the internal (vibrational) temperature of the dimer is estimated to be $\approx 30\,K$. At this temperature a population of only the lowest four vibrational states [21] of the electronic ground state $^1\Sigma_g^+$ of the dimer is significant (see figure 1). Taking these states into account the internuclear separation of the target dimers is distributed as shown in the inset of figure 1. It extends from $\approx 3.4\,\text{Å}$ to $\approx 4.7\,\text{Å}$.

After collimation the supersonic beam was intersected by a Ti:sapphire laser beam at right angles in its focal spot where a light intensity of $\approx 2 \times 10^{14}\,W\,cm^{-2}$ was reached (see figure 2). The pulse repetition rate of the Ti:sapphire laser was 3 kHz. The laser pulses had a full width at half maximum (FWHM) of 5.5 fs and a central wavelength of $\approx 770\,nm$. The carrier–envelope (CE) phase of these pulses was not stable. Photoelectron momentum distributions thus are an average over all possible values of the CE phase.
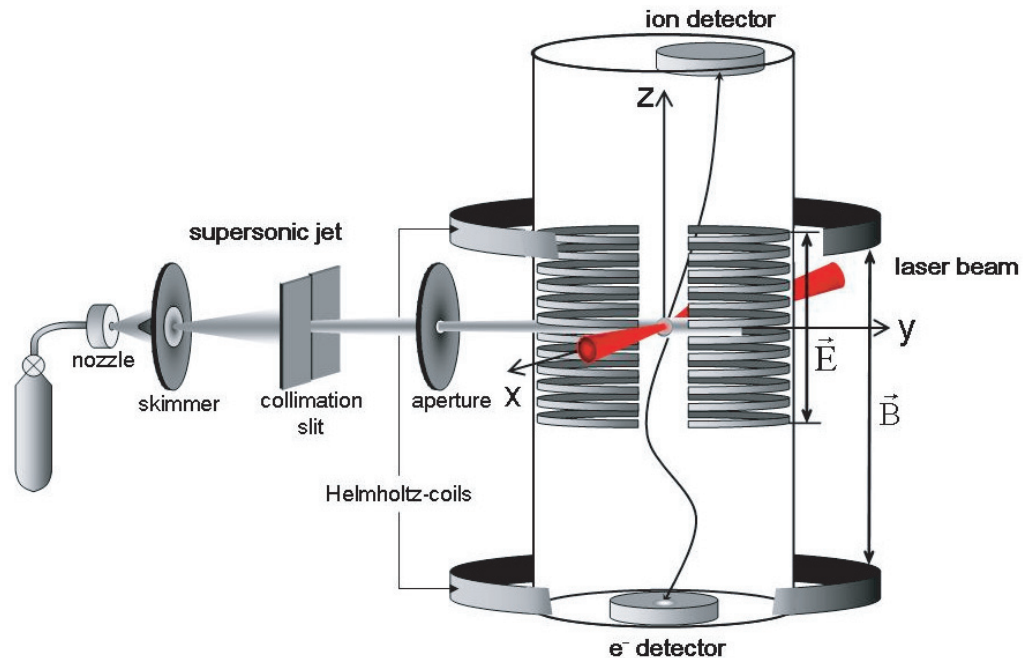
Figure 2. The reaction microscope setup.

A weak homogeneous electric field ($7.5\,\mathrm{V\,cm^{-1}}$) was applied across the interaction region to extract photoelectrons and ions (figure 2). After acceleration and subsequent field-free drift they were detected by position sensitive multichannel plate detectors. A homogeneous magnetic field of $8.5\,\mathrm{G}$ parallel to the electric field guided all photoelectrons to the detector. Thus a 4π solid angle of detection is reached for ions and electrons. For each particle the time-of-flight was determined along with the position where it hit the detector. From these data the full momentum vector of each individual particle can be reconstructed.

The experiment recorded the momentum distributions of photoelectrons from the ionization processes:

$$\mathrm{Ar} \rightarrow \mathrm{Ar^+ + e,}$$
$$\mathrm{Ar_2} \rightarrow \mathrm{Ar_2^+ + e.}$$
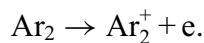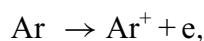
To be able to identify whether a photoelectron hitting the detector is coming from ionization of an Ar atom or an $\mathrm{Ar_2}$ dimer the corresponding photoion (either $\mathrm{Ar^+}$ or $\mathrm{Ar_2^+}$) was detected together with each electron. For an unambiguous correspondence we restricted the rate of detecting photoelectrons to $\approx20\%$ of the repetition rate of the laser pulses. Due to the predominant abundance of Ar atoms in the supersonic beam an electron detected together with an $\mathrm{Ar^+}$ ion comes from an Ar atom ionization event. An electron detected together with an $\mathrm{Ar_2^+}$ ion either comes from photoionization of an $\mathrm{Ar_2}$ dimer or possibly from dissociative ionization of a higher Ar cluster with formation of an $\mathrm{Ar_2^+}$ fragment. An $\mathrm{Ar_2^+}$ ion from $\mathrm{Ar_2}$ photoionization only gets recoil momentum from photoionization, whereas an $\mathrm{Ar_2^+}$ ion from dissociative ionization of a higher cluster gains additional momentum from the dissociation process. Although our estimate of the cluster fraction (Ar_n, $n > 2$) in the supersonic beam already resulted in a negligible value (see above) we use momentum conservation in photoionization to further justify that
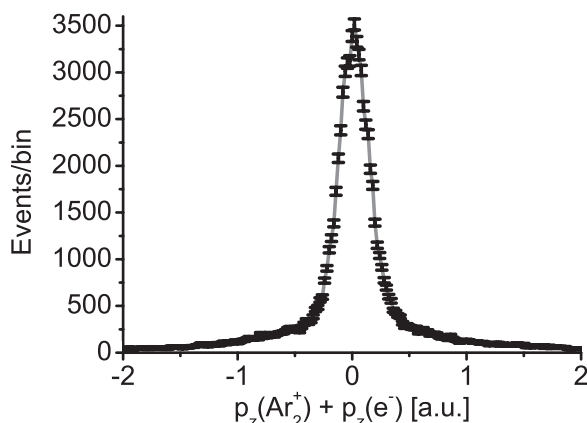
Figure 3. The distribution of the z-component of the sum-momentum of Ar_2^+ ions and the corresponding photoelectron for events where an Ar_2^+ ion is detected together with a photoelectron.

spurious contributions to the photoelectron spectrum of fragmentation of Ar_n ($n > 2$) clusters into Ar_2^+ and a photoelectron are not significant. In the case of Ar_2 photoionization the sum of the ion and photoelectron momenta is equal to the momentum of the argon dimer in the supersonic beam which got ionized. For our geometry (see the setup in figure 2) this means that the sum $p_z(Ar_2^+) + p_z(e) = 0$ for the z-components of the momenta of the ion $p_z(Ar_2^+)$ and of the photoelectron $p_z(e)$. In figure 3, the distribution of this sum-momentum (z-component) is plotted for those events where an Ar_2^+ ion was detected together with a photoelectron. Indeed, it can be seen that a narrow peak develops at $p_z(Ar_2^+) + p_z(e) = 0$ with a width (FWHM) of 0.31 au. The small background on both sides is caused mainly by false coincidences. The width of the peak is determined by the Ar_2^+ momentum resolution of our setup. The sum–momentum component of (Ar_2^+, e) pairs along the z-axis is thus practically zero. For dissociative ionization of higher clusters ($Ar_n \rightarrow Ar_{n-2} + Ar_2^+ + e$), we would have expected to find a broad sum-momentum distribution for the (Ar_2^+, e) pairs since it is just equal to the momentum of the neutral dissociation product Ar_{n-2}. However, such events are not found in the experiment. Therefore, we can virtually exclude that dissociative ionization of higher argon clusters (Ar_n, $n > 2$) contributes to the events within this peak. Admitting only photoelectrons to the Ar_2 photoelectron spectrum that come together with an Ar_2^+ ion also prevents dissociative ionization of Ar_2 from contributing to the measured photoelectron momentum distribution. The detection technique used allowed to take the photoelectron momentum distributions for strong-field ionization of Ar atoms and Ar_2 dimers in the same experimental run and thus under completely identical experimental conditions.

3. Theoretical considerations

A possible effect of interference on the momentum distribution of photoelectrons from strong-field ionization of the Ar_2 dimer can be derived from the strong-field approximation (SFA) to the transition matrix element to the continuum [25]. Using either the velocity-gauge or the dressed length-gauge molecular SFA that was introduced in [25] it is possible to factorize the SFA transition matrix element for the dimer into an atomic transition matrix element and an

interference term. The simple factorization works for the contribution of the directly emitted photoelectrons to the momentum distribution. These are the electrons which did not encounter rescattering from the Ar_2^+ ion core after they entered the ionization continuum. In the case of the Ar_2 dimer with a large internuclear separation and very small interaction between the atomic constituents it is expected that especially the dressed molecular SFA is a reasonable approximation to describe strong-field ionization [25, 26]. Factorization of the transition matrix element allows one to calculate dimer momentum distributions easily from measured monomer distributions without the necessity to evaluate the atomic transition matrix element. This significantly simplifies a comparison of the theoretically expected dimer momentum distribution with the actually measured one.

The lowest lying Ar_2^+ states which may be reached by strong-field ionization are shown in figure 1 (data from [22]). They arise from removal of an electron from a $3p\sigma_u$, $3p\pi_g$, $3p\pi_u$ or $3p\sigma_g$ orbital, respectively [27]. Spin–orbit interaction gives rise to a coupling of the open shell Ar_2^+ states and thus to the level structure in figure 1 [22]. Only ejection of an electron from the $3p\sigma_u$ and $3p\pi_g$ orbitals results in a stable Ar_2^+ ion [22]. Thus, only these have to be taken into account in an SFA analysis at first sight. However, the spin–orbit coupling in the ion complicates the situation. Bound ionic states which may be reached by strong-field ionization within the Franck–Condon regime (see figure 1) are I(1/2)U, II(1/2)U and I(3/2)G. The latter one corresponds to removal of an electron from the $3p\pi_g$ orbital exclusively, whereas removal of an electron from the $3p\sigma_u$ and the $3p\pi_u$ orbitals together contributes to the I(1/2)U and II(1/2)U states. Thus, one should also consider the $3p\pi_u$ molecular orbital for a more thorough analysis.

We construct the molecular initial state orbitals by linear combination of unperturbed atomic ones. This is a reasonable assumption in the Franck–Condon regime (see figure 1). In the derivation of the factorization we assume that the atomic orbital aligned along the laser polarization axis (magnetic quantum number $m_l = 0$) alone contributes significantly to strong-field ionization of the Ar atom. This assumption is well justified as shown in [28]. For the $3p\sigma_u$, $3p\pi_u$ and $3p\pi_g$ orbitals we then arrive at the following factorization of the molecular SFA matrix element using the velocity gauge [25]:

$$M_{fi,M}^{3p\sigma_u}(\mathbf{p}, \mathbf{R}) = 2 S_{v_f, v_i} M_{fi,A}^{3p0}(\mathbf{p}) \cos\theta_R \cos(\mathbf{p} \cdot \mathbf{R}/2), \tag{1}$$

$$M_{fi,M}^{3p\pi_u}(\mathbf{p}, \mathbf{R}) = -2 S_{v_f, v_i} M_{fi,A}^{3p0}(\mathbf{p}) \sin\theta_R \cos(\mathbf{p} \cdot \mathbf{R}/2), \tag{2}$$

$$M_{fi,M}^{3p\pi_g}(\mathbf{p}, \mathbf{R}) = -2i S_{v_f, v_i} M_{fi,A}^{3p0}(\mathbf{p}) \sin\theta_R \sin(\mathbf{p} \cdot \mathbf{R}/2). \tag{3}$$

S_{v_f, v_i} is the Franck–Condon factor for transition from a specific vibrational state in the Ar dimer to a final vibrational state in Ar_2^+. $M_{fi,A}^{3p0}(\mathbf{p})$ is the atomic SFA matrix element for ionization of an Ar 3p-electron and θ_R the angle between the internuclear axis and the direction of polarization of the laser pulse which is assumed to be linear. In (1)–(3) $R = |\mathbf{R}|$ is the equilibrium internuclear separation in the initial vibrational state v_i of the dimer. The factorization above assumes that the Franck–Condon principle is applicable. This is justified since the **R**-dependent terms in the equations above do not change significantly in the photoelectron momentum range relevant in the experiment when R varies over the internuclear separations present in the dimer beam in the experiment (see the inset in figure 1). Using the more involved dressed length-gauge molecular SFA instead of the velocity-gauge to evaluate the transition matrix element gives rise to the same factorization as given above.

The interference factors $\cos(\mathbf{p} \cdot \mathbf{R}/2)$ and $\sin(\mathbf{p} \cdot \mathbf{R}/2)$ appearing in the factorization in (1)–(3), respectively, are well known from short wavelength photoionization after absorption of a single photon [10]–[13] and for ionization in collision processes [5]–[9]. The additional terms $\cos \theta_R$ and $\sin \theta_R$ arise from the specific molecular orbital where the electron is removed. The behaviour of the interference terms in (1)–(3) is completely different. In the case of the $3p\sigma_u$ and $3p\pi_u$ orbitals the two centres of the molecule emit in phase. This gives rise to a maximum in the interference term at $\mathbf{p} = \mathbf{0}$. On the other hand, for the $3p\pi_g$ orbital the two centres emit out of phase by π. This leads to a zero in the interference term at $\mathbf{p} = \mathbf{0}$ (see (3)).

In the experiment the internuclear axis of the sample is not aligned at a certain angle with respect to the light polarization vector. It is thus necessary to average $|M_{\mathrm{fi,M}}^{3p\sigma_u}(\mathbf{p}, \mathbf{R})|^2$, $|M_{\mathrm{fi,M}}^{3p\pi_u}(\mathbf{p}, \mathbf{R})|^2$ and $|M_{\mathrm{fi,M}}^{3p\pi_g}(\mathbf{p}, \mathbf{R})|^2$ over all orientations of the internuclear axis to get the experimentally observable relation between the monomer and the dimer momentum distributions. In the Ar_2 sample all orientations appear with the same probability. Averaging then yields:

$$\overline{\left| M_{\mathrm{fi,M}}^{3p\sigma_u}(\mathbf{p}, \mathbf{R}) \right|^2} = \left| 2S_{v_f,v_i} \right|^2 \left| M_{\mathrm{fi,A}}^{3p0}(\mathbf{p}) \right|^2 \left[\frac{1}{6} + \frac{1}{2} \int \frac{\mathrm{d}\Omega_{\hat{\mathbf{R}}}}{4\pi} \cos(\mathbf{p} \cdot \mathbf{R}) \cos^2 \theta_R \right], \tag{4}$$

$$\overline{\left| M_{\mathrm{fi,M}}^{3p\pi_u}(\mathbf{p}, \mathbf{R}) \right|^2} = \left| 2S_{v_f,v_i} \right|^2 \left| M_{\mathrm{fi,A}}^{3p0}(\mathbf{p}) \right|^2 \left[\frac{1}{3} + \frac{\sin(pR)}{2pR} - \frac{1}{2} \int \frac{\mathrm{d}\Omega_{\hat{\mathbf{R}}}}{4\pi} \cos(\mathbf{p} \cdot \mathbf{R}) \cos^2 \theta_R \right], \tag{5}$$

$$\overline{\left| M_{\mathrm{fi,M}}^{3p\pi_g}(\mathbf{p}, \mathbf{R}) \right|^2} = \left| 2S_{v_f,v_i} \right|^2 \left| M_{\mathrm{fi,A}}^{3p0}(\mathbf{p}) \right|^2 \left[\frac{1}{3} - \frac{\sin(pR)}{2pR} + \frac{1}{2} \int \frac{\mathrm{d}\Omega_{\hat{\mathbf{R}}}}{4\pi} \cos(\mathbf{p} \cdot \mathbf{R}) \cos^2 \theta_R \right]. \tag{6}$$

The remaining integral in these relations can be done analytically:

$$\int \frac{\mathrm{d}\Omega_{\hat{\mathbf{R}}}}{4\pi} \cos(\mathbf{p} \cdot \mathbf{R}) \cos^2 \theta_R = \frac{\sin^2 \theta}{2} \frac{\sin pR}{pR} + \left[\cos^2 \theta - \frac{\sin^2 \theta}{2} \right]$$
$$\times \left[\frac{2}{(pR)^2} \cos pR + \left(\frac{1}{pR} - \frac{2}{(pR)^3} \right) \sin pR \right],$$

with θ the angle enclosed between the photoelectron momentum vector and the direction of polarization of the laser pulse. The averaged results depend only on the internuclear separation R and on the momentum $\mathbf{p}$ of the photoelectron. The interference factors in square brackets depend explicitly on the angle of ejection of the photoelectron with respect to the polarization axis of the laser pulse. Averaging over the orientation of the internuclear axis reduces the influence of interference on the photoelectron momentum distribution significantly. The main effect survives close to $\mathbf{p} = \mathbf{0}$ in a momentum range determined by $pR < 3\pi/2$ where R is the equilibrium internuclear separation of Ar_2. The larger R is, the smaller the corresponding momentum range.

4. Experimental results and discussion

Strong-field ionization of the argon dimer in a 5.5 fs laser pulse assures nuclear motion in Ar_2 to be virtually frozen during interaction with the pulse. The laser pulse thus interacts
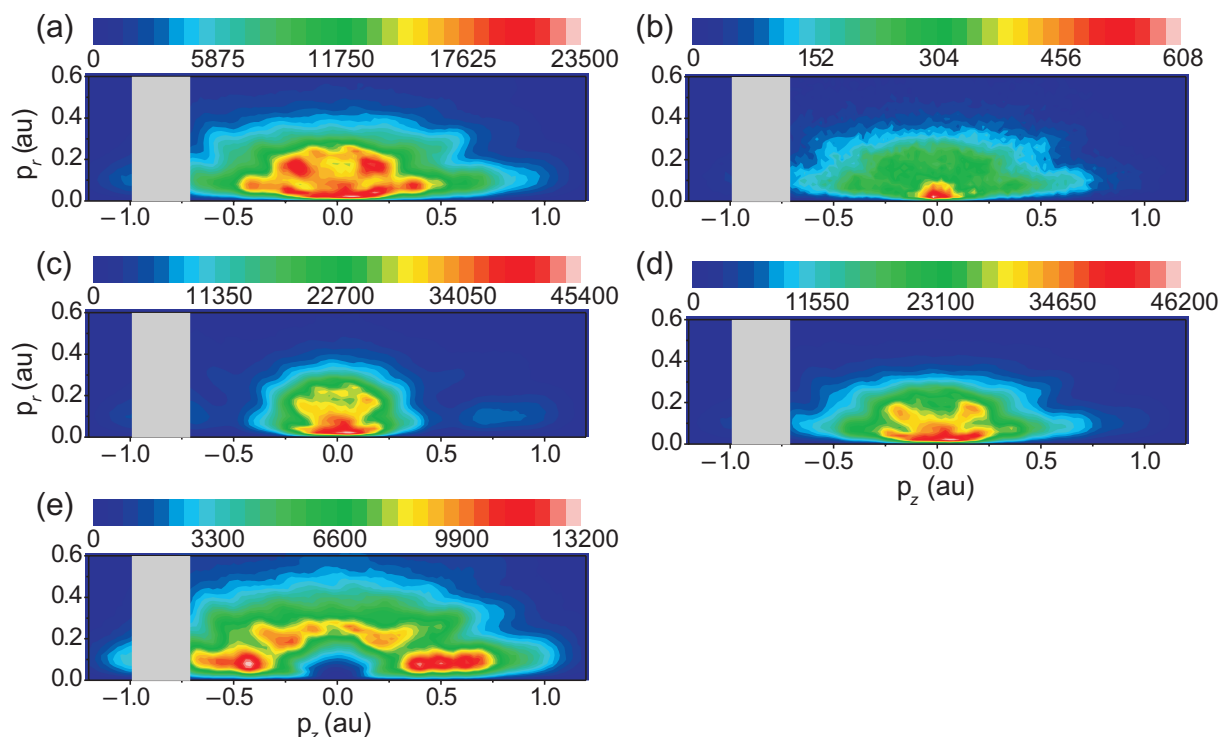
Figure 4. Measured photoelectron momentum distributions for strong-field ionization of: (a) Ar and (b) Ar_2. The laser field is linearly polarized along the p_z axis (intensity: $\approx 2 \times 10^{14}$ W cm^{-2}). p_r and p_z are the cylindrical components of the photoelectron momentum vector. Simulated momentum distributions for Ar_2 are shown in (c) based on equation (4), in (d) based on (5), and in (e) based on (6), assuming a $3p\sigma_u$, a $3p\pi_u$, or a $3p\pi_g$ electron of Ar_2 is ionized, respectively. The internuclear separation used in the simulation is $R = 3.77$ Å. The grey bar covers a momentum range with degraded resolution.

with a randomly aligned ensemble of dimers distributed over internuclear separations around a mean value R (see the inset in figure 1). Figure 4(a) shows the measured Ar photoelectron momentum distribution and figure 4(b) the corresponding spectrum for Ar_2 at a laser pulse peak intensity of $\approx 2 \times 10^{14}$ W cm^{-2}. Only photoionization events with $|p_z(Ar_2^+) + p_z(e)| < 0.45$ au (see figure 3) have been included in the Ar_2 photoelectron momentum distribution. This assures that only photoionization of Ar_2 from the channel $Ar_2 \rightarrow Ar_2^+ + e$ contributes and not dissociative photoionization of higher clusters and of Ar_2 (see the discussion above). Cylindrical coordinates are used, with the laser pulse linearly polarized along the p_z-axis. In the figure the number of events detected per momentum bin ($\delta p_r \delta p_z$) are shown (bin size: $\delta p_r = \delta p_z = 0.02$ au). This gives rise to a zero appearing along the p_z-axis ($p_r = 0$) due to the accessible phase space volume which decreases to zero proportional to p_r. All distributions are integrated over the azimuthal angle because of cylindrical symmetry with respect to the polarization vector. The spectra have been recorded 'simultaneously' (see section 2) under completely identical experimental conditions, but they obviously look significantly different. For atomic argon, the distribution is spread out along the p_z and p_r axes, whereas the Ar_2 spectrum exhibits a narrow 'spike' near zero momentum.
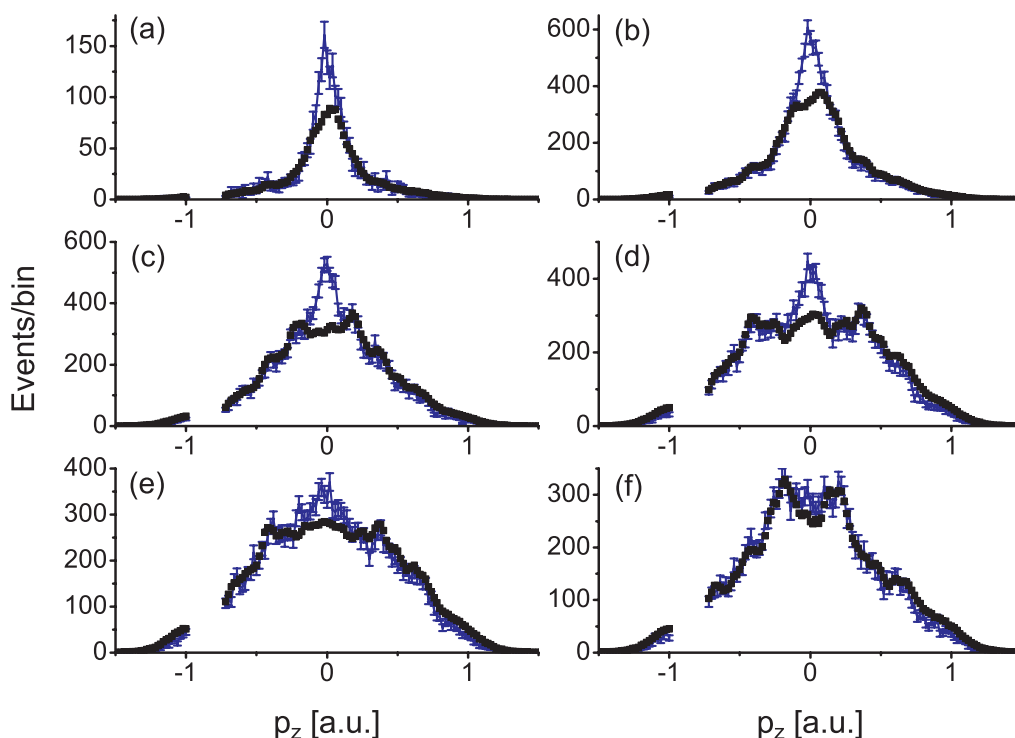
Figure 5. Cuts through the measured 2D atomic ((black) squares) and dimer (full (blue) line with error bars) momentum distributions of figure 4 at fixed p_r parallel to the p_z-axis. (a) $p_r = 0.01 \pm 0.01$ au, (b) $p_r = 0.03 \pm 0.01$ au, (c) $p_r = 0.05 \pm 0.01$ au, (d) $p_r = 0.09 \pm 0.01$ au, (e) $p_r = 0.11 \pm 0.01$ au, and (f) $p_r = 0.15 \pm 0.01$ au. Missing points between $p_z = -1$ au and $p_z = -0.7$ au indicate the momentum range with degraded resolution.

For a quantitative comparison figure 5 shows representative cuts through the measured two-dimensional (2D) distributions along the p_z-axis at successively increasing radial momentum component p_r (black squares: Ar, full blue line with error bars: Ar_2). The cuts have been made at: (a) $p_r = 0.01 \pm 0.01$ au, (b) $p_r = 0.03 \pm 0.01$ au, (c) $p_r = 0.05 \pm 0.01$ au, (d) $p_r = 0.09 \pm 0.01$ au, (e) $p_r = 0.11 \pm 0.01$ au, and (f) $p_r = 0.15 \pm 0.01$ au. On the vertical axis the number of electrons detected per momentum bin together with an Ar_2^+ ion is plotted. The error bars give the statistical error margin. The Ar^+ spectrum is scaled by a factor 0.016. This scaling matches the measured atom and dimer momentum distribution cuts along the p_z-axis for all $p_r > 0.15$ au. In this momentum regime the functional dependences of the momentum distributions for Ar and Ar_2 on p_z are practically identical. The main difference between the spectra is found for $|\mathbf{p}| \leqslant 0.15$ au, i.e. it is confined to photoelectron kinetic energies smaller than 0.3 eV. Similar to figure 5, figure 6 shows one representative radial cut through the 2D momentum distributions at $p_z = 0 \pm 0.01$ au. On the vertical axis again the number of Ar_2 ionization events per momentum bin is plotted. The scaling factor for the Ar spectrum is the same as in figure 5. This cut confirms the result found for the cuts along the p_z-axis.

We expect the main difference between the Ar and Ar_2 photoelectron momentum distributions to be caused by two-centre interference. To check this expectation, we used relations (4)–(6) to construct momentum distributions for ionization of the Ar_2 dimer by
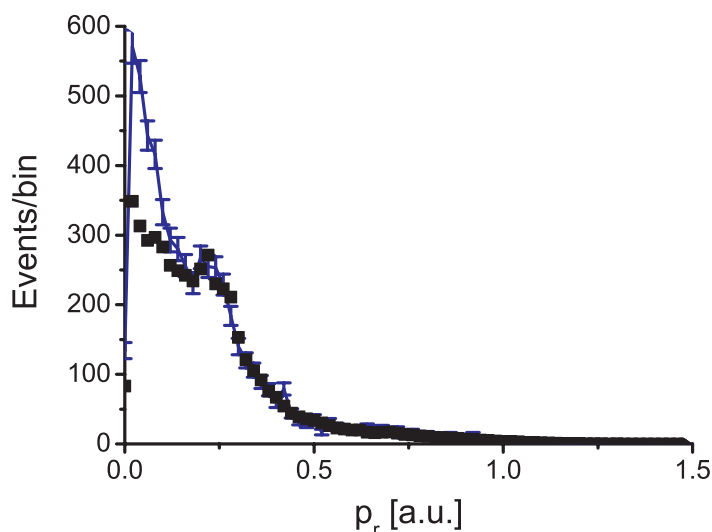
Figure 6. Radial cuts through the measured 2D atomic ((black) squares) and dimer (full (blue) line with error bars) momentum distributions of figure 4 at fixed $p_z = 0 \pm 0.01$ au.

plugging in the measured Ar momentum distribution. In this way the possible contribution of each individual orbital to the momentum distribution is unveiled. Figures 4(c)–(e) show the contributions of the $3p\sigma_u$, $3p\pi_u$ and $3p\pi_g$ orbitals, respectively. Only electrons removed from these orbitals contribute to the electronic states I(1/2)U, II(1/2)U and I(3/2)G of Ar_2^+ which support bound vibrational levels in the Franck–Condon regime of the ionization transition (see figure 1). Only these electrons are detected in the experiment. In this range of internuclear separations the energy difference between the electronic states is less than ≈ 0.64 eV. One thus expects that all three will be populated in the strong-field ionization process since no selection rules exist.

As can already be seen in figure 4 a superposition of contributions from these orbitals will not reproduce the measured dimer momentum distribution (figure 4(b)) exactly. The two ungerade orbitals $3p\sigma_u$ and $3p\pi_u$ tend to form the 'spike' at $\mathbf{p} = \mathbf{0}$ that is found in the experiment. However, the width of the central maximum appears to be too wide in the simulated spectra. The emptied $3p\pi_g$ orbital which makes up the I(3/2)G ionic state shows a hole in the momentum distribution around $\mathbf{p} = \mathbf{0}$ where the ungerade orbitals form the 'spike'. Removal of an electron from this orbital contributes to the momentum distribution at large momenta. As can be seen from equations (5) and (6) an equal contribution of both orbitals, $3p\pi_u$ and $3p\pi_g$, would erase the interference completely. The same holds for the $3p\sigma_u$ and $3p\sigma_g$ orbitals.

A quantitative comparison of measured and simulated dimer spectra via cuts through the 2D distributions confirms the qualitative result. Representative cuts along the p_z-axis at several radial momenta p_r are shown in figure 7. In each graph the full blue line with error bars shows the measured Ar_2 electron momentum distribution. The cuts shown have been made at $p_r = 0.01 \pm 0.01$ au (figures 7(a) and (b)), $p_r = 0.05 \pm 0.01$ au (figures 7(c) and (d)), $p_r = 0.09 \pm 0.01$ au (figures 7(e) and (f)), and at $p_r = 0.15 \pm 0.01$ au (figures 7(g) and (h)). The full black lines in each graph represent the corresponding cuts through the simulated dimer spectra with an electron removed from the $3p\sigma_u$ orbital (relation (4)) in figures 7(a), (c), (e)
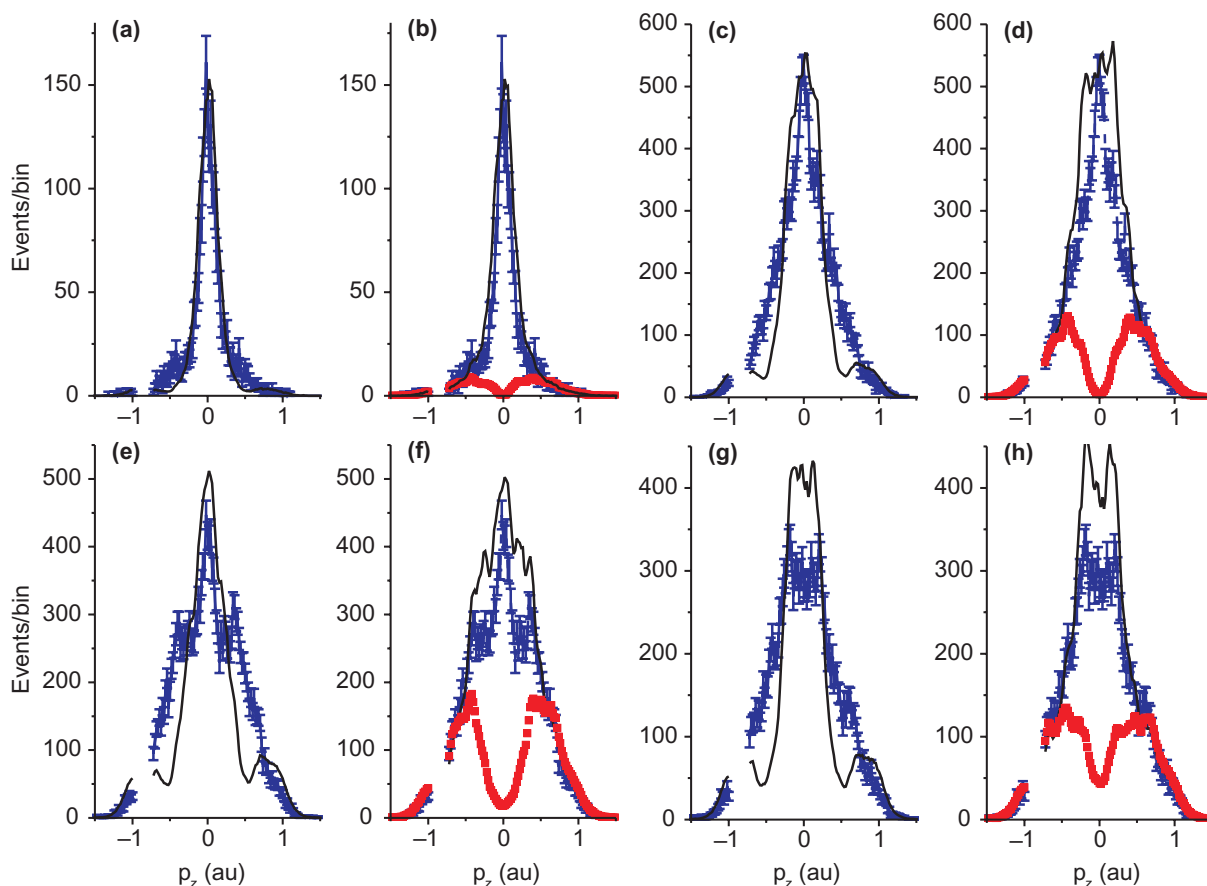
Figure 7. Comparison of cuts along the p_z-axis through the 2D measured dimer momentum distribution (blue lines with error bars) with the simulated spectra using the factorization relations: (4) $3p\sigma_u$ orbital: black lines in (a), (c), (e) and (g); (5) $3p\pi_u$ orbital: black lines in (b), (d), (f) and (h); (6) $3p\pi_g$ orbital: red squares in (b), (d), (f) and (h). The $3p\sigma_u$ and $3p\pi_u$ simulated distributions have been normalized once to the measured Ar_2 spectrum in the cut at $p_r = 0.01$ au ((a) and (b)) for $p_z = 0$. No specific normalization was attempted for the $3p\pi_g$ spectra. Cuts shown are made at the radial momenta $p_r = 0.01 \pm 0.01$ au ((a) and (b)), $p_r = 0.05 \pm 0.01$ au ((c) and (d)), $p_r = 0.09 \pm 0.01$ au ((e) and (f)) and $p_r = 0.15 \pm 0.01$ au ((g) and (h)).

and (g), and with the electron removed from the $3p\pi_u$ orbital (relation (5)) in figures 7(b), (d), (f) and (h). Removal of the electron from the $3p\pi_g$ orbital gives rise to the simulated cuts shown as red squares in figure 7(b), (d), (f) and (h). The $3p\sigma_u$ and $3p\pi_u$ simulated spectra have been normalized once to the measured dimer spectrum at $p_r = 0.01$ au and $p_z = 0$ (see figures 7(a) and (b)). No normalization of the $3p\pi_g$ spectra has been done.

In figure 7(a) the simulated $3p\sigma_u$ spectrum fits quite well the central 'spike' in the measured Ar_2 spectrum. However, already for $|p_z| > 0.4$ au visible deviations from the measurement appear. The deviations become sizeable for the cuts at larger p_r. A similar behaviour is found for removal of the electron from the $3p\pi_u$ orbital. It is also not possible to reduce the deviations to a reasonably small value in the whole spectral range (less than the statistical error bars in the Ar_2
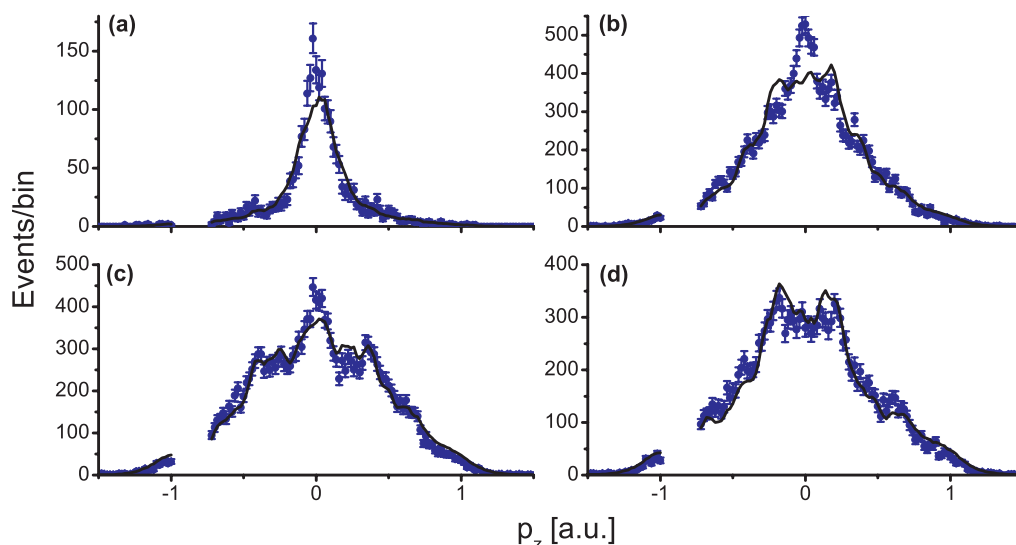
Figure 8. Least squares fit (full black line) of a sum of simulated Ar_2 momentum distributions to the measured Ar_2 photoelectron momentum distribution (blue dots with error bars). Cuts shown are made at the radial momenta $p_r = 0.01 \pm 0.01$ au (a), $p_r = 0.05 \pm 0.01$ au (b), $p_r = 0.09 \pm 0.01$ au (c) and $p_r = 0.15 \pm 0.01$ au (d). The least square fit was made for graph (c). The simulated spectra for all other cuts use the same fit parameters as in (c).

spectrum) by assuming that removal of an electron from all three orbitals ($3p\sigma_u$, $3p\pi_u$ and $3p\pi_g$), suitably weighed, contributes to the measured dimer spectrum. This can be seen in figure 8. We used the simulated cuts along the p_z-axis for the $3p\sigma_u$, $3p\pi_u$ and $3p\pi_g$ orbitals at $p_r = 0.09$ au for a least square fit to the measured momentum distribution at this radial momentum. The best fit is found by weighting the contributions with the factors $a(3p\sigma_u) = 0.11$, $a(3p\pi_u) = 0.57$ and $a(3p\pi_g) = 0.32$. For all four cuts shown in figure 8 the same weighting factors for the different contributions have been used. The fit is shown as a black line and the measured dimer momentum distribution as dots with error bars. Specifically the central maximum of the measured momentum distribution is not reproduced well by the fit.

The simulation of the dimer momentum distribution, assuming the difference from the Ar spectrum is caused by interference, already converges to the measured Ar_2 momentum distribution. This strongly points to interference actually being the origin for the difference in the spectra. However, as pointed out, a full agreement over the whole accessible momentum space cannot be reached. Thus, the question regarding the origin of the residual deviations arises. The factorization of the two-centre transition matrix element (equations (1)–(3)) is based on certain assumptions and approximations: the SFA is applied, only photoelectrons leaving the dimer directly without rescattering are taken into account, and electron dynamics in the Ar_2^+ ion, which may even be driven by the strong laser pulse, is not considered.

The SFA ignores the existence of excited states of the dimer except for the ionization continuum. It thus does not account for the possible influence of excited bound states on strong-field ionization and therefore on the photoelectron spectrum. The presence of a possible influence was discussed in [29] in connection with electric field ionization of H_2 at large internuclear separation. This system is similar to the Ar_2 dimer investigated here. In a static

electric field at field strengths comparable to the one reached in the laser pulses we used, a strong enhancement in the diabatic ionization rate is observed at internuclear separations near 6 au [29]. This is brought about by the fact that besides the electronic ground state of H_2 a state based on the ionic configuration H^+H^- gains importance. In Ar_2, we start strong-field ionization just in the range of internuclear separations in question. A transient formation of Ar^+Ar^- in the laser pulse may modify the ionization process and may possibly influence the momentum distribution of the photoelectrons.

The factorization uses a Volkov propagator for the final state in the matrix element [25]. It is thus assumed that the evolution in time of the final state is not influenced by the Coulomb interaction with the residual Ar_2^+ ion core. This interaction may either modify the interference term in the factorization or even preclude an exact factorization with relations (1)–(3) only being a first approximation. In the Ar atom the influence of the Coulomb interaction is actually noticeable as shown in [30].

The SFA used for the derivation of the factorization is based on the strong-field matrix element that encompasses only the direct transition to the continuum through electric field ionization of the dimer [25]. It does not include the possibility of elastic rescattering of the electron on the Ar_2^+ ion core. For the Ar atom it is known that rescattering contributes to the photoelectron spectrum only at a level which is approximately two orders of magnitude lower than the contribution of the directly emitted electrons [31]. It is noticeable only at a photoelectron momentum component p_z, parallel to the laser polarization axis, which is larger than $\approx 2\sqrt{U_p}$ (U_p is the ponderomotive energy of the photoelectron in the laser field). $2\sqrt{U_p}$ is just the upper limit of the classical drift momentum an electron can gain from the laser field. The contribution of directly emitted electrons to the spectrum becomes small beyond this limit. In our case $2\sqrt{U_p} \cong 1.28$ au. Provided this fact can be transferred to the Ar_2 dimer one would expect the contribution from elastic rescattering in the low momentum range relevant here to be of minor importance.

However, for the dimer the situation may be different. In Ar_2 the electrons are localized at the atomic constituents. Thus, strong-field (tunnel) ionization of the dimer means one of the atoms is ionized. In each optical cycle tunnel ionization happens most probably close to a maximum of the electric field strength. The electron in the continuum is then accelerated by the electric field of the laser pulse. Using the classical equations of motion and ionization times close to the field strength maxima, the first rescattering possibility on the Ar^+ ion core where the electron was removed may happen after a time between $\approx T/2$ and T has elapsed. T is the optical period of the pulse which in our case is 2.57 fs. It is also possible to estimate the time it takes the electron to reach the not ionized atom in the dimer for the first time. At the light intensity of 2×10^{14} W cm^{-2} present in the experiment and the internuclear separation of ≈ 7 au this happens about $0.15T$ after tunnel ionization. This is the time for dimers with the internuclear axis aligned along the direction of polarization of the laser pulse. This time is significantly shorter than the time it takes to rescatter on the Ar^+ ion core where the electron started. The spread of the electron wavepacket when scattering on the Ar atom constituent is thus significantly smaller than its spread when rescattering on the Ar^+ ion. Assuming a width of the wavepacket transverse to the electric field of the laser pulse at tunnel time of 2 au one estimates that the current incident on the Ar atom is approximately 10–20 times higher than the current hitting the Ar^+ ion. The elastic scattering cross sections for the Ar atom and Ar^+ ion are quite similar [32, 33]. Thus, one may expect that elastic scattering on the Ar atom may actually contribute 10–20 times more to the photoelectron momentum distribution than elastic

rescattering on the Ar^+ ion. In view of the rescattering contribution in the case of strong-field ionization of an Ar atom one may expect a scattering contribution on the Ar atom in the dimer on a level larger than 10% of the contribution of the directly emitted electrons. Since the differential elastic scattering cross section on Ar peaks near forward scattering [32] one may even expect that a significant change in the photoelectron momentum distribution appears in the momentum range $p_z < 2\sqrt{U_p}$ and therefore close to $\mathbf{p} = \mathbf{0}$. This is just where we find significant residual deviations of the measured momentum distribution from the simulated spectrum when taking into account only the electrons emitted directly which do not scatter internally.

The situation found here may be similar to that observed for photoionization of the $1\sigma_g$ and $1\sigma_u$ inner shell electrons of the N_2 molecule by absorption of a single high-energy photon [12, 13]. In [12, 13] a significant contribution of internally scattered electrons to the photoelectron spectrum was observed. It appears to be responsible for a considerable phase shift of the observed interference oscillations in the dependence of the ionization cross section of these orbitals on the photon energy with respect to the position one determines by assuming only electrons without internal scattering are emitted from the molecule.

It should be mentioned that an improved molecular SFA which includes rescattering of the ionized electron on the atomic (ionic) centres has recently been introduced in [34]. Numerical results have shown a significant modification of the high-energy angle-resolved electron spectra of N_2 and O_2 molecules compared to the spectra of their companion atoms (Ar and Xe). This is caused by the interference of four rescattering paths contributing to the transition matrix element. However, the method developed in [34] was applied only to high-energy electrons and should be reconsidered if one wants to apply it to the above-discussed internal electron scattering.

In view of the potential energy curves of the Ar_2^+ ion in figure 1 one final point has to be considered. The largest energy separation between the electronic states is 0.64 eV in the Franck–Condon regime for transitions from the Ar_2 electronic ground state (figure 1). This means that all these final ionic states will participate in strong-field ionization of the Ar_2 dimer. Thus, a certain dynamic evolution in time is induced in the ion, the outcome of which may have an influence on the measured photoelectron momentum distribution. While the laser pulse is applied, nuclear motion (vibration and rotation) is completely frozen. Only electron dynamics is relevant. This is an electron charge oscillation in the ion which is induced if one assumes that ionization of the dimer is practically ionization of one of the two constituent, nearly unperturbed Ar atoms. According to this point of view a non-stationary superposition of ionic states is excited. In the Franck–Condon regime the minimum period of this charge oscillation is ≈ 6.5 fs corresponding to the largest energy splitting of 0.64 eV (see figure 1). Therefore, over one period of the laser pulse (≈ 2.6 fs) a considerable electron charge displacement in the ion may happen. This is the same timescale on which the internal collisions of the tunnel ionized electron occur (see above). It may thus be expected that the recollision dynamics is influenced by the internal electron dynamics in the Ar_2^+ ion which in turn may appear in the electron momentum distribution.

So far it has been assumed that the ionic electron dynamics occurs in an unperturbed way. This may be an oversimplification in view of the energy splittings present in the ion, the fact that the ionic states are charge resonance states with a strong dipole coupling [22], and the laser pulse peak intensity is high. The laser pulse may thus drive transitions between these states after ionization of the dimer. This will have an influence on the outcome of population over the ionic states and thus on the momentum distribution of photoelectrons coming together with an Ar_2^+ ion. This discussion shows that it is probably necessary to take the electron dynamics in the

ion into account in order to get a precise description of the strong-field ionization process and therefore of the photoelectron momentum distribution.

5. Summary

In conclusion, noble gas dimers in general and Ar_2 specifically are ideal systems to investigate molecular strong-field phenomena at large internuclear separation. Promoting an electron to the ionization continuum occurs here with the highest probability close to one of the atomic sites which constitute virtually unperturbed atoms. One thus expects the photoelectron spectrum to be mainly determined by two-centre interference of two virtually 'independent' atomic emitters. Actually, we find differences between the Ar and Ar_2 photoelectron momentum distributions which can be attributed to two-centre interference. They are localized close to zero electron momentum since we are using an unaligned dimer sample. Averaging over the orientation of the internuclear axis damps the interference for electron momenta p larger than $\approx 3\pi/(2R)$ (here $\approx 0.67\,\mathrm{au}$) to a level smaller than the statistical error margin in the experiment. The situation would improve for dimers aligned with respect to the laser pulse polarization vector. Here, the damping would vanish completely (see equations (1)–(3)) and the interference would influence the whole photoelectron momentum distribution.

The experimental results also show that for a complete description of the dimer photoelectron momentum distribution it is not sufficient to assume Ar_2 to consist of two coherent, basically atomic, electron emitters which are simply electric field ionized by the high intensity infrared laser pulse. The SFA factorization of the dimer transition matrix element into an atomic part and an interference factor that we introduced thus has to be improved. We identified several contributions to the matrix element which may have a significant influence on the momentum distribution and should be considered in a future theoretical analysis of strong-field ionization of the Ar_2 dimer: elastic rescattering of the electron on the Ar_2^+ ion core, the possible influence of excited states of the neutral dimer on strong-field ionization, Coulomb interaction of the photoelectron with the residual Ar_2^+ ion core (in the final state), and electron charge oscillations induced in the ion core. We expect that all noble gas dimers behave similar to the Ar_2 dimer and that it may even be possible to generalize our results to all diatomic molecules provided their internuclear separation is large enough to be able to view their ionization as ionization of a two basically independent atoms.

The deviations from basic two-centre interference we found in the experiment may open up the chance to get insight into the dimer electron dynamics during strong-field ionization in future investigations. Provided tunnel ionization of the dimer is practically identical to promoting an electron to the continuum at one of the atomic sites, a charge oscillation in the ion is inevitably initiated. Its timescale is of the order of the oscillation period of the laser radiation. Thus, an influence on the rescattering dynamics of the photoelectron on the Ar_2^+ ion may be expected. The dynamics of this charge oscillation and its possible coupling to the outgoing photoelectron motion is highly interesting in itself.

Acknowledgments

References

[1] Young T 1804 *Phil. Trans. R. Soc.* **94** 1
[2] Jönsson C 1961 *Z. Phys.* **161** 454
[3] Estermann I and Stern O 1930 *Z. Phys.* **61** 95
[4] Arndt M, Nairz O, Vos-Andreae J, Keller C, Van der Zouw G and Zeilinger A 1999 *Nature* **401** 680
[5] Kamalou O, Chesnel J-Y, Martina D, Hanssen J, Stia C R, Fojón O A, Rivarola R D and Frémont F 2005 *Phys. Rev.* A **71** 010702
[6] Galassi M E, Rivarola R D, Fainstein P D and Stolterfoht N 2002 *Phys. Rev.* A **66** 052705
[7] Stolterfoht N, Sulik B, Skogvall B, Chesnel J Y, Frémont F, Hennecart D, Cassimi A, Adoui L, Hossain S and Tanis J A 2004 *Phys. Rev.* A **69** 012701
[8] Misra D, Kadhane U, Singh Y P, Tribedi L C, Fainstein P D and Richard P 2004 *Phys. Rev. Lett.* **92** 153201
[9] Hossain S, Landers A L, Stolterfoth N and Tanis J A 2005 *Phys. Rev.* A **72** 010701
[10] Cohen H D and Fano U 1966 *Phys. Rev.* **150** 30
[11] Rolles D *et al* 2005 *Nature* **437** 711
[12] Liu X-J *et al* 2006 *J. Phys. B: At. Mol. Opt. Phys.* **39** 4801
[13] Liu X-J, Prümper G, Gel'mukhanov F, Cherepkov N A, Tanaka H and Ueda K 2007 *J. Electron Spectrosc. Relat. Phenom.* **156–158** 73
[14] Lindner F, Schätzel M G, Walther H, Baltuska A, Goulielmakis E, Krausz F, Milošević D B, Bauer D, Becker W and Paulus G G 2005 *Phys. Rev. Lett.* **95** 040401
[15] Grasbon F, Paulus G G, Chin S L, Walther H, Muth-Böhm J, Becker A and Faisal F H M 2001 *Phys. Rev.* A **63** 041402
[16] Eremina E, Liu X, Rottke H, Sandner W, Schätzel M G, Dreischuh A, Paulus G G, Walther H, Moshammer R and Ullrich J 2004 *Phys. Rev. Lett.* **92** 173001
[17] Jaroń-Becker A, Becker A and Faisal F H M 2006 *Phys. Rev. Lett.* **96** 143006
[18] Lein M, Hay N, Velotta R, Marangos J P and Knight P L 2002 *Phys. Rev.* A **66** 023805
[19] Vozzi C *et al* 2006 *J. Phys. B: At. Mol. Opt. Phys.* **39** S457
[20] Itatani J, Levesque J, Zeidler D, Niikura H, Pépin H, Kieffer J C, Corkum P B and Villeneuve D M 2004 *Nature* **432** 867
[21] Slaviček P, Kalus R, Paška P, Odvárková I, Hobza P and Malijevský A 2003 *J. Chem. Phys.* **119** 2102
[22] Wadt W R 1978 *J. Chem. Phys.* **68** 402
[23] Ullrich J, Moshammer R, Dorn A, Dörner R, Schmidt L Ph H and Schmidt-Böcking H 2003 *Rep. Prog. Phys.* **66** 1463
[24] Miller D R 1988 Free Jet Sources *Atomic and Molecular Beam Methods* vol 1 ed G Scoles (Oxford: Oxford University Press) pp 14–53
[25] Milošević D B 2006 *Phys. Rev.* A **74** 063404
[26] Becker W, Chen J, Chen S G and Milošević D B 2007 *Phys. Rev.* A **76** 033403
[27] Stevens W J, Gardner M, Karo A and Julienne P 1977 *J. Chem. Phys.* **67** 2860
[28] Ammosov M V, Delone N B and Krainov V P 1986 *Zh. Eksp. Teor. Fiz.* **91** 2008
[29] Saenz A 2000 *Phys. Rev.* A **61** 051402
[30] Rudenko A, Zrost K, Ergler Th, Voitkiv A B, Najjari B, de Jesus V L B, Feuerstein B, Schröter C D, Moshammer R and Ullrich J 2005 *J. Phys. B: At. Mol. Opt. Phys.* **38** L191
[31] Paulus G G, Nicklich W, Xu H, Lambropoulos P and Walther H 1994 *Phys. Rev. Lett.* **72** 2851
[32] McEachran R P and Stauffer A D 1983 *J. Phys. B: At. Mol. Phys.* **16** 4023
[33] Brotton S J, McKenna P, Gribakin G and Williams I D 2002 *Phys. Rev.* A **66** 062706
[34] Busuladžić M, Gazibegović-Busuladžić A, Milošević D B and Becker W 2008 *Phys. Rev. Lett.* **100** 203003